

Inversion of flow and heat transfer of the paramagnetic fluid in a differentially heated cube

Kenjereš, S.; Fornalik-Wajs, E.; Wrobel, W.; Szmyd, J. S.

DOI

[10.1016/j.ijheatmasstransfer.2020.119407](https://doi.org/10.1016/j.ijheatmasstransfer.2020.119407)

Publication date

2020

Document Version

Final published version

Published in

International Journal of Heat and Mass Transfer

Citation (APA)

Kenjereš, S., Fornalik-Wajs, E., Wrobel, W., & Szmyd, J. S. (2020). Inversion of flow and heat transfer of the paramagnetic fluid in a differentially heated cube. *International Journal of Heat and Mass Transfer*, 151, Article 119407. <https://doi.org/10.1016/j.ijheatmasstransfer.2020.119407>

Important note

To cite this publication, please use the final published version (if applicable). Please check the document version above.

Copyright

Other than for strictly personal use, it is not permitted to download, forward or distribute the text or part of it, without the consent of the author(s) and/or copyright holder(s), unless the work is under an open content license such as Creative Commons.

Takedown policy

Please contact us and provide details if you believe this document breaches copyrights. We will remove access to the work immediately and investigate your claim.



Inversion of flow and heat transfer of the paramagnetic fluid in a differentially heated cube

S. Kenjereš^{a,*}, E. Fornalik-Wajs^b, W. Wrobel^b, J.S. Szmyd^b

^aTransport Phenomena Section, Department of Chemical Engineering, Faculty of Applied Sciences and J. M. Burgers Center for Fluid Mechanics, Delft University of Technology, Van der Maasweg 9, Delft 2629 HZ, The Netherlands

^bDepartment of Fundamental Research in Energy Engineering, Faculty of Energy and Fuels, AGH University of Science and Technology, 30 Mickiewicz Avenue, Krakow 30059, Poland

ARTICLE INFO

Article history:

Received 7 December 2018

Revised 9 January 2020

Accepted 20 January 2020

Keywords:

Heat transfer control

Paramagnetic fluid

Thermomagnetic convection

Magnetization force

ABSTRACT

The present study addresses the detailed numerical analysis of the flow and heat transfer of a paramagnetic fluid inside a differentially heated cubical box and subjected to a strong non-uniform magnetic field. Two different heating scenarios are considered regarding an initial thermal stratification: unstable (heated from the bottom) and stable (heated from the top), both subjected to the same magnetic field. For a fixed value of the thermal Rayleigh number ($Ra = 1.4 \times 10^5$) integral heat transfer is measured over a range of imposed magnetic fields, $0 \leq |b_0|_{\max} \leq 10$ T. To obtain detailed insights into local wall-heat transfer and its dependency on the flow patterns generated, numerical simulations of the experimental setup are performed. A relatively good agreement between experiments and numerical simulations is obtained in predicting the integral heat transfer (with an averaged $\Delta Nu < 7\%$ over the entire range of working parameters for both heating configurations). It is demonstrated that a strong convective motion can be generated under the influence of the magnetization force even for the heated-from-above situation that initially was in the pure conduction state. This magnetically assisted (heated from the bottom) and magnetically inverted (heated from the top) Rayleigh-Bénard convection produced up to 5 and 15 times more efficient heat transfer compared to the initial neutral situation, respectively.

© 2020 The Authors. Published by Elsevier Ltd.

This is an open access article under the CC BY-NC-ND license.

(<http://creativecommons.org/licenses/by-nc-nd/4.0/>)

1. Introduction

In the pioneering work of Braithwaite et al. [1], the authors presented for the very first time, by performing experiments with paramagnetic fluids, the manner in which the magnetic convection can be generated by strong magnetic gradients available in superconducting magnets. Application of the strongest magnetic field in a heated from the bottom and cooled from the top configuration resulted in approximately 2.5 times increase of the integral heat transfer in comparison to the neutral situation. It was suggested that this concept of heat transfer control might be potentially used in heat transfer devices or crystal growth control.

A detailed review of various research directions and results regarding the use of the thermomagnetic convection in technological applications (material processing, magnetic Czochralski crystal growing system) was presented in [2].

The numerical simulations of thermo-magnetic convection in cylindrical cells of different aspect ratios (1:2 and 1:0.5) filled with non-conducting or low-conducting paramagnetic fluids were presented in [3]. For the magnetic assisting case of heated from bottom and cooled from the top configuration (of an aspect ratio of 1:2), authors reported the maximum heat transfer and maximum velocity increase of 15% and 60%, respectively, when compared to the neutral situation. For the differentially side-heated cavity with an aspect ratio of 1:0.5, the magnetically supporting case increased the Nusselt number and maximum velocity of 17% and 25%, respectively. For the same configuration, magnetically suppressing case revealed a local minimum in the Nu versus magnetic field strength curve. Finally, it was concluded that the magnetic buoyancy force could be applied for controlling convection and enhancing the heat transfer efficiency.

In numerical studies of [4–7], it was demonstrated that even 'normal fluids' such as air or water could be influenced by magnetization forces when sufficiently strong magnetic field gradients were generated in the new generation of the superconducting magnets (up to 5 T in the center of the magnet bore).

* Corresponding author.

E-mail address: s.kenjeres@tudelft.nl (S. Kenjereš).

Nomenclature

a	thermal diffusivity (m^2/s)
p	pressure (Pa)
r	distance from a current-carrying wire (m)
g_i	gravity vector (m/s^2)
u_i	velocity vector (m/s)
u, v, w	velocity vector components in the x -, y - and z -direction (m/s)
b_i	magnetic field induction (T)
b_0	magnetic field magnitude (T)
f_i^P	pressure force (N/kg)
f_i^B	thermal-buoyancy force (N/kg)
f_i^M	magnetization force (N/kg)
q_{loss}	heat loss (W)
q_{heater}	heat produced by heater (W)
q_{cond}	pure conduction heat transfer (W)
$q_{\text{cond}}^{\text{theoretical}}$	theoretical pure conduction heat transfer (W)
D, H, L	characteristic enclosure dimensions (m)
I	electric current (A)
V	voltage (V)
V_b	buoyancy velocity (m/s)
Nu	Nusselt number (–)
Ra	Rayleigh number (–)
Pr	Prandtl number (–)
h	hot
c	cold
ρ	density (kg/m^3)
ν	kinematic viscosity (m^2/s)
μ	dynamic viscosity (Pa s)
μ_m	magnetic permeability (H/m)
χ_0	magnetic susceptibility (–)
β	thermal expansion coefficient ($1/\text{K}$)
γ	magnetization number (–)
λ	thermal conductivity ($\text{W}/\text{m K}$)
θ	temperature (K)
θ_0	reference temperature (K)

Because of its simplicity and inherently steady flow regimes (for low values of the Rayleigh number), the side-heated cube with a paramagnetic fluid was investigated in [8–10]. The integral heat transfer was measured and compared with numerical simulations, which were performed on a rather coarse numerical mesh of 42^3 , Bednarz et al. [8]. Due to some numerical stability issues of the used numerical solver, lower values of Prandtl number were simulated than in experiments. The first qualitative visualizations of the temperature in the central vertical plane were also reported, but without a direct comparison with the numerical results obtained. A two-fold increase of the integral heat transfer was reported for the strongest magnetic field ($b_0 = 5$ T). The direct comparison of temperature fields was presented in [9].

Measurements of total heat transfer and qualitative visualizations of temperature for a bottom-heated cube, but without numerical simulations, were presented in [10]. The experimentally determined heat transfer enhancement of factor two was reported for the strongest magnetic field (5 T) (in respect to the neutral case).

A different configuration was studied in [11] where a vertical annular enclosure with a heated inner and cooled outer cylinder was analyzed for different angles of inclination and different strengths of the imposed magnetic field (up to 10 T in the center of magnet bore). Measured and numerically obtained Nusselt numbers were compared, and a good agreement was obtained. The non-monotonic behavior of the Nusselt number was reported, i.e.

when the magnetic field was activated, after an initial suppression and reaching a critical minimal value of the Nusselt number, a gradual increase was observed. The location of the this minimal heat transfer was a case specific. For the configuration placed at the edge of the magnetic coil, the following pattern in Nusselt numbers was observed: $\text{Nu} = 5$ (for $|b_0|_{\text{max}} = 0$ T), 3 (for $|b_0|_{\text{max}} = 2$ T) and 9 (or $|b_0|_{\text{max}} = 10$ T), respectively. In contrast to this, for the configuration placed in the magnetic coil center, the following pattern in Nusselt number was obtained: $\text{Nu} = 5$ (for $|b_0|_{\text{max}} = 0$ T), 4 (for $|b_0|_{\text{max}} = 3$ T) and 7 (or $|b_0|_{\text{max}} = 10$ T), respectively.

The oscillatory flow and heat transfer regimes were presented for the very first time in [12], in which the paramagnetic fluids with a range of the Prandtl number were used in combined experimental and numerical studies. The measured integral heat transfer was significantly enhanced in the presence of the strong magnetic field ($b_0 = 10$ T) for all considered values of Prandtl number, i.e. $\text{Nu}_b/\text{Nu}_0 = 3.3, 3.25$ and 4.1 for $\text{Pr} = 584, 120$ and 20 , respectively.

Finally, the fully developed turbulent regimes of the thermomagnetic convection (Rayleigh-Bénard-Kelvin convection) were reported in [13]. For the highest applied strength of the magnetic field ($b_0 = 10$ T) and the lowest value of the simulated Prandtl number ($\text{Pr} = 5.84$), the maximal heat transfer enhancement of $\text{Nu}_b/\text{Nu}_0 = 4.5$ was obtained.

In the present paper, we revisit the simple cubical enclosure configuration filled with a paramagnetic fluid, and experimentally and numerically investigate two initial thermal stratification cases - heated from the top and heated from the bottom - both under the same imposed magnetic field (up to 10 T). We would like to analyze to what extent the flow and heat transfer of the initially pure conduction regime (the heated-from-the-top) can be modulated and to compare it to the heated-from-the-bottom case. In parallel to the experiments, where the integral heat transfer is measured, we also perform highly resolved numerical simulations to provide detailed insights into the reorganization of the flow and temperature, as well as the local heat transfer in the proximity of thermally active walls. The major novelty of the presented research lies in this combination of the experimental and highly resolving numerical simulation approach (however, the numerical part determines the character of the present work), covering two different initial orientations of the temperature gradients. For both, experiments and numerical simulations, the level of high magnetic induction value (up to 10 T) allows an extension of the results range previously published. The numerical approach also includes analysis of the local wall heat transfer and profiles of the thermal-buoyancy and magnetization forces for the very first time.

2. Experimental set-up

2.1. Cubical box

The experimental cubical box (with $L = H = D = 0.032$ m) is constructed to provide an easily controllable heating or cooling of the thermally active horizontal walls, which are made from copper plates, Fig. 1(a). The remaining four side walls are made from plexiglass. The heating is done by a rubber-coated nichrome wire placed just under the heated plate. The voltage and electric current for the nichrome wire are recorded by two multi-meters. The cooling is achieved by running water through a constant temperature bath. The temperatures of the copper plates are measured by the T-type sheath thermocouples inserted into small holes inside the plates. The used thermocouples are shielded, which made it possible to operate in the strong magnetic field.

The cubical box is filled with the paramagnetic fluid consisting of 80% mass aqueous solution of glycerol in which gadolinium nitrate hexahydrate ($\text{Gd}(\text{NO}_3)_3 \cdot 6\text{H}_2\text{O}$) is dissolved to a concen-

Table 1

Properties of the working paramagnetic fluid (water with 80% volume glycerine solution and 0.8 mol [Gd(NO₃)₃ · 6H₂O]).

Properties	Symbol	Value	Unit
Density	ρ	1463 ± 1	kg/m ³
Dynamic viscosity	μ	86.89 × 10 ⁻³ ± 0.064 × 10 ⁻³	Pa s
Magnetic susceptibility	χ_0	3.37 × 10 ⁻⁴ ± 0.001 × 10 ⁻⁴	–
Thermal expansion coefficient	β	0.52 × 10 ⁻³	1/K
Thermal conductivity	λ	0.397	W/m K
Thermal diffusivity	a	1.01 × 10 ⁻⁷	m ² /s
Prandtl number	Pr	584	–

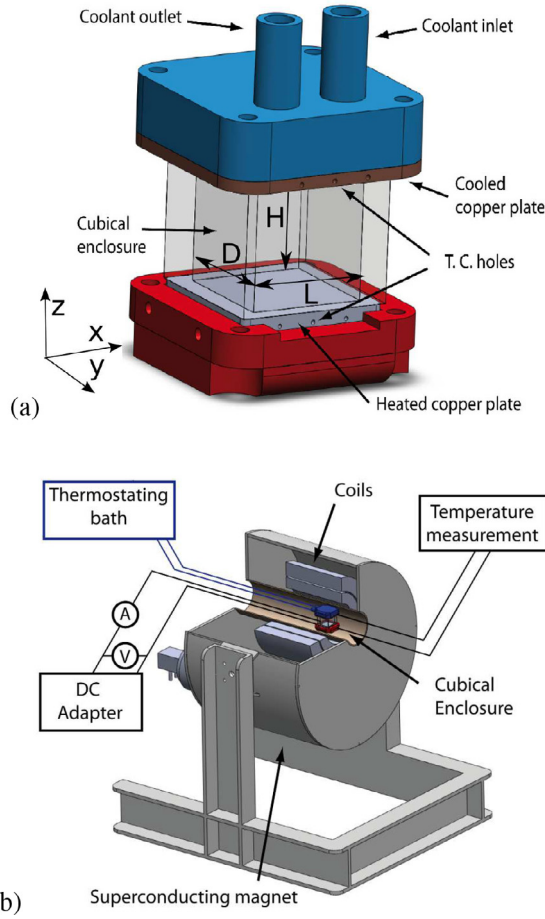


Fig. 1. A sketch of the cubical enclosure with copper plates filled with paramagnetic fluid (a), and superconducting magnet (b) with the location of the cube in the magnet bore.

tration of 0.8 mol/kg. The physical properties of the working fluid are either measured at room temperature (quantities indicated by ± measuring accuracy) or estimated from the literature [8,14] and are given in Table 1.

The integral heat transfer coefficient (Nusselt number) is calculated as a ratio between the net convective heat transfer rate and the net pure conduction contribution, Churchill and Ozoe [15]. The pure conduction experiments (heated-from-the-top configuration) are performed with various values of the total electric power supply for a nichrome wire heater, and the temperature difference between the hot and cold walls is measured. By using the known thermal diffusion of the working fluid, the net thermal conduction heat flux can be estimated for each temperature difference. The heat losses (q_{loss}) are calculated from the total heat supply and are used to create a heat loss line for the pure conduction exper-

iments, i.e. $q_{loss} = q_{cond} - q_{cond}^{theoretical}$, with theoretical pure conduction calculated as $q_{cond}^{theoretical} = \lambda H \Delta \theta$. Experiments show that these heat losses can be approximated as $q_{loss} \propto 0.08 \Delta \theta$ for temperature differences in the $2.5 \leq \Delta \theta \leq 16$ K range. In the next step, convection experiments are conducted and the heat loss for each temperature difference yields the net convection heat transfer rate. Finally, the ratio between the net convection and net pure conduction is obtained as [15]:

$$Nu = \frac{q_{heater} - q_{loss}}{q_{cond}^{theoretical}} = \frac{I \cdot V - q_{loss}}{\lambda \frac{\Delta \theta}{H} DL} = \frac{I \cdot V - q_{loss}}{\lambda \Delta \theta H} \quad (1)$$

where I is the electric current and V is the voltage of the heater regulator. Experiments with supplied heat rate of $q_{heater} = 0.4$ W, with temperatures of cooled and heated copper plates of 291 K and 296 K, respectively, are used for direct comparison with numerical simulations for both heating configurations (heating from the top or heating from the bottom).

2.2. Superconducting magnet

In the present research, superconducting helium free magnet is used (model HF10-1-VHT-B, produced by Sumitomo Heavy Industries, Ltd., Japan), [11–13]. The basic characteristics of this superconducting magnet are the maximal magnetic induction up to 10 T (in the center of the magnet bore), and with magnetic induction gradients up to 900 T/m² (at the edges of the magnet bore). The magnet bore has a diameter of 0.1 m and a length of 0.5 m. The superconducting magnet can rotate around the center of axis providing great flexibility in making various mutual orientations of the imposed magnetic field gradients and the gravity vector. In the present study, we adopt the horizontal orientation of the superconducting magnet axis and placing of the cube filled with paramagnetic fluid at the edge of the magnet coils within the center of the axis of the magnet bore, Fig. 1(b). This placement makes a 90° orientation between the gravity vector (acting in the z-direction) and the main magnetic field gradient (acting in the x-direction). It is expected that this orientation will generate a dominant magnetization force in the horizontal direction, which will lead to an inverted flow and heat transfer (similar to the classical heated-from-side case) in comparison with the neutral situation, i.e. without the imposed magnetic field.

3. Numerical simulations

3.1. Mathematical model

The system of equations describing the flow and heat transfer of a paramagnetic working fluid subjected to a strong external non-uniform magnetic field consists of the conservation laws for mass, momentum, and energy. The extended momentum and energy equations can be written as:

$$\frac{\partial u_i}{\partial t} + u_j \frac{\partial u_i}{\partial x_j} = \frac{\partial}{\partial x_j} \left[\nu \left(\frac{\partial u_i}{\partial x_j} + \frac{\partial u_j}{\partial x_i} \right) \right] + f_i^p + f_i^b + f_i^M \quad (2)$$

$$\frac{\partial \theta}{\partial t} + u_j \frac{\partial \theta}{\partial x_j} = \frac{\partial}{\partial x_j} \left(a \frac{\partial \theta}{\partial x_j} \right) \quad (3)$$

where additional forces are the pressure force (f_i^P) thermal buoyancy (f_i^B) and magnetization force (f_i^M). These forces (per unit mass) can be expressed as:

$$f_i^P = -\frac{1}{\rho} \frac{\partial p}{\partial x_i}, \quad (4)$$

$$f_i^B = -\beta g_i (\theta - \theta_0), \quad (5)$$

$$f_i^M = -\left(1 + \frac{1}{\beta \theta_0}\right) \frac{\chi_0 \beta (\theta - \theta_0)}{2\mu_m} \frac{\partial |b_0|^2}{\partial x_i} \quad (6)$$

where the Boussinesq approximation is used to express the thermal buoyancy and magnetization forces. The later is modeled by considering magnetic susceptibility as a function of temperature, Tagawa et al. [4]. The momentum and temperature equation together with the divergency-free conditions for velocity and magnetic field

$$\frac{\partial u_i}{\partial x_i} = 0, \quad \frac{\partial b_i}{\partial x_i} = 0 \quad (7)$$

form the fully closed system of equations. The magnetic field distribution is calculated from Biot-Savart's law for a current-carrying coil as [16]:

$$\mathbf{b} = \frac{\mu_m I}{4\pi} \int \frac{d\mathbf{s} \times \mathbf{r}}{r^3} \quad (8)$$

where I is the strength of the electric current, r is the distance from a wire and $d\mathbf{s}$ is the length of the differential element of the current-carrying wire. We consider the one-way coupling between the imposed magnetic field and fluid flow, i.e., the imposed magnetic field does not change in time. Note that despite a constant value of the imposed magnetic field, the magnetization force (f_i^M) is not constant since it depends on the local temperature (Eq. (6)) (similarly to the thermal buoyancy force). Although we solve the system of Eqs. (2)–(7) in its dimensional form, it is important to introduce three characteristic dimensionless parameters which determine the physics of the problem considered:

- $Ra = \beta g \Delta \theta \text{Pr}(\rho/\mu)^2 H^3$, the Rayleigh number,
- $\gamma = \chi_0 |b_0|_{\max}^2 / \mu_m g H$, the magnetization number,
- $\text{Pr} = \nu/a$, the Prandtl number.

Note that the $|b_0|_{\max}$ represents the maximum of the modulus of the imposed magnetic field in the center of the magnetic bore. In the present study, we kept the temperature difference between thermally active horizontal plates at a constant level, $\Delta \theta = 5$ K, that gives the value of the thermal buoyancy Rayleigh number of $Ra = 1.4 \times 10^5$. The magnetization number that represents a ratio between magnetization and gravitational force is in $0 \leq \gamma \leq 60$ range.

3.2. Calculation of magnetic field

The spatial distribution of the imposed magnetic field is calculated from the discretised form of Eq. (8) by using the identical finite-volume approach as used for the flow and heat transfer transport variables. We mimic the real superconducting magnet structure which includes two coils made of the superconducting wires operating at the cryogenic temperature. Different strengths of the magnetic field are obtained by regulating the electric current intensity through the coils. We generate a database containing the spatial distribution of the magnetic field for various intensities of the magnetic field strength, i.e., $0 \leq |b_0|_{\max} \leq 10$ T. Distributions

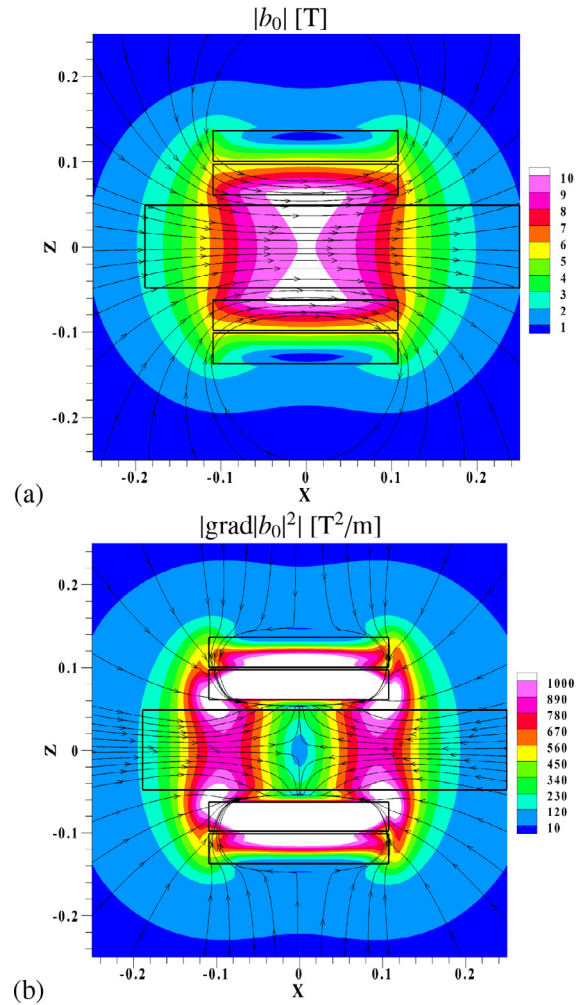


Fig. 2. The magnetic flux lines and contours of the magnetic field magnitude (in T) (a) and flux lines of magnetic field gradients and contours of the magnitude of the magnetic field gradient (in T^2/m) (b). The central rectangle indicates the bore inside the magnet and coils are indicated with remaining four rectangles. Note that the used coordinate system is for the entire simulated set-up.

of the highest generated magnetic field and its main gradient are illustrated in Fig. 2. Note that the cube is inserted such that its center coincides with the right edge of the coils, i.e., at approximately 0.1 m from the magnet bore center. Since the magnetic field does not change in time, its magnitude and gradients are loaded only once during the pre-processing phase of simulations after the generation of the numerical mesh. Contours of the modulus of the magnetic field gradient at the highest values of the imposed magnetic field at $|b_0|_{\max} = 10$ T are shown in Fig. 3a. Similarly, characteristic profiles of the modulus of the magnetic field gradient in the central vertical plane of the cubical box for different strengths of the imposed magnetic field ($0 \leq |b_0|_{\max} \leq 10$ T) are plotted in Fig. 3b.

3.3. Numerical method

The system of Eqs. (2)–(7) is discretised and iteratively solved by an in-house three-dimensional finite-volume based Navier-Stokes numerical solver for general non-orthogonal geometries, Kenjereš [12,13,17]. The convective and diffusive terms of conservative equations are discretised by the second-order central-difference scheme (CDS). The time integration is performed with a fully-implicit second-order three-consecutive time-step scheme.

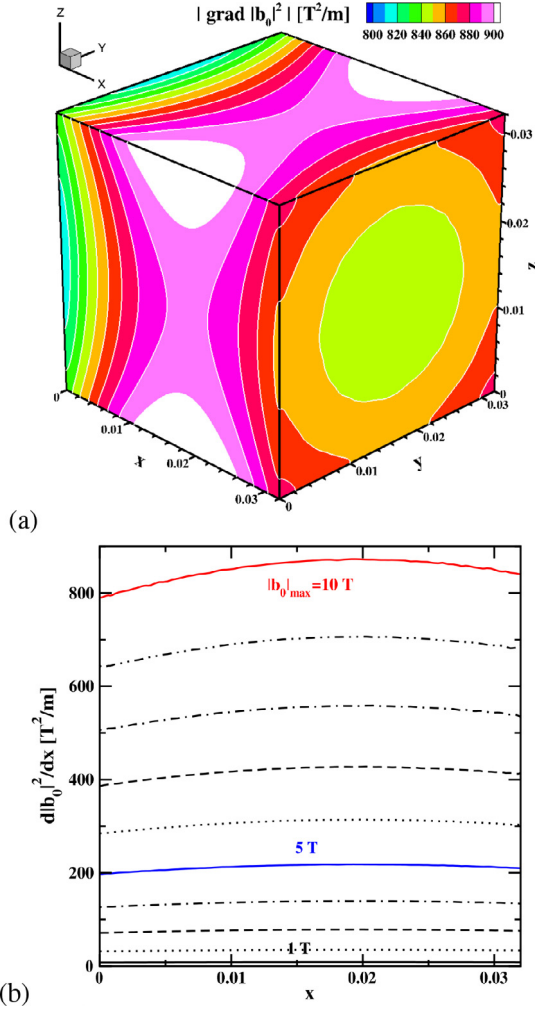


Fig. 3. Contours of the modulus of the magnetic field square gradient within the cubical box for $|b_0|_{\max} = 10$ T working conditions (a). Profiles of the horizontal gradient of the square of the magnetic field ($d|b_0|^2/dx$) in the central horizontal plane ($y_c = 0.016$ m, $z_c = 0.016$ m) for entire range of $1 \leq |b_0|_{\max} \leq 10$ T (b). Note that used coordinate system is for the cubical box only.

The numerical solver is used in parallel mode using the Message Passing Interface (MPI) domain decomposition based directives. A non-uniformly distributed hexagonal control volumes represent the cubical box interior. The numerical mesh used varied between 82^3 , 102^3 , 122^3 , 162^3 and 182^3 control volumes. All results presented here are obtained with 122^3 numerical mesh with the characteristic non-dimensional thickness of the very first row of the cells in the proximity of thermally active walls of $z_{\text{wall}}/H = 0.00375$. This value is selected such that from estimated thickness of the thermal boundary layer (calculated from $\delta_\theta = H/(2Nu) \approx 10^{-3}$ m, Grötzbach [18]) we have placed at least five control volumes to properly resolve the steep temperature gradient in the conductive sublayer. This mesh design proved to provide grid-independent solutions for highest applied magnetic field strength (the difference in integral Nusselt number is less than 0.5% between 122^3 and 182^3 mesh). Note that for such a case, the strongest flow is also generated due to an enhancing mechanism of the imposed magnetic gradients, making us conclude that this numerical resolution will also be sufficient for the weaker magnetic fields. All simulations were performed as a time-dependent, with a typical value of the time-step estimated as $\Delta t = t^*/100 \approx 0.05$ s, with $t^* = 4H/V_b$ as characteristic eddy (convective structure) turnover time, and $V_b = \sqrt{\beta g \Delta \theta H}$ as characteristic buoyancy velocity.

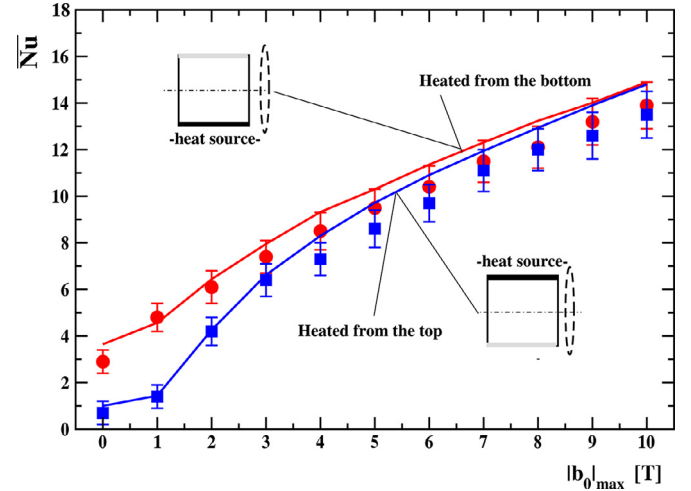


Fig. 4. Integral Nusselt number for a cubical enclosure of a paramagnetic fluid ($Pr = 584$) heated from the top (blue color) or from bottom (red color) for different strengths of the imposed magnetic field ($|b_0| = 0, \dots, 10$ T) from horizontal coil orientation of superconducting magnet. Experimental data - symbols with error bars, numerical simulations - lines. (For interpretation of the references to color in this figure legend, the reader is referred to the web version of this article.)

ity. Note that smaller value of the time-step $\Delta t = 0.01$ s provided identical results, confirming that obtained results are time-step independent.

4. Results and discussion

4.1. Heat transfer

We start our analysis by comparing experimentally and numerically obtained long-term time-averaged integral heat transfer (Nusselt number) for different initial configurations subjected to different strengths of the imposed magnetic field gradients, Fig. 4.¹ The heated-from-top configuration (blue lines and symbols), due to its stable initial thermal stratification, for a neutral case (magnetic field switched-off, $|b_0|_{\max} = 0$ T) produced a pure conductive state, i.e., no convective motion was observed. By increasing the magnetic field strength, enhancement of the integral heat transfer is observed for both initially differentially heated configurations. For the range of high intensities of imposed magnetic fields, $|b_0|_{\max} \geq 8$ T, there is a relatively small difference between the heated-from-the-top and heated-from-the-bottom configurations. This is an indicator that a fully inverted convection took place for the initially thermally stable configuration, and, practically, the same efficiency of the heat transfer is achieved for both cases. Overall, it can be seen that qualitatively good agreement is obtained between experiments and simulations. The averaged difference between measured and numerically calculated Nusselt number is $\Delta \bar{Nu} < 7\%$ over the entire range of working parameters for both configurations. Some deviations are observed in the upper range of the imposed magnetic fields. This can be due to some unaccounted heat losses in the experimental set-up or possible viscosity dependence of the working fluid on the local temperature and the imposed magnetic field (i.e. $\mu = \mu(\theta, b_i)$) that was not taken into account in the present numerical model. Distributions of the local Nusselt number along the horizontal heated

¹ Note that experimentally determined integral Nusselt number was calculated from Eq. (1), whereas the simulated value was calculated as: $Nu^{\text{sim}} = 1/L \int_0^L \left(1/D \int_0^D Nu_{\text{local}}(x, y) dy \right) dx$, with the local Nusselt number calculated as: $Nu_{\text{local}}(x, y) = \partial \theta / \partial z|_{\text{wall}} H / (\theta_h - \theta_c)$.

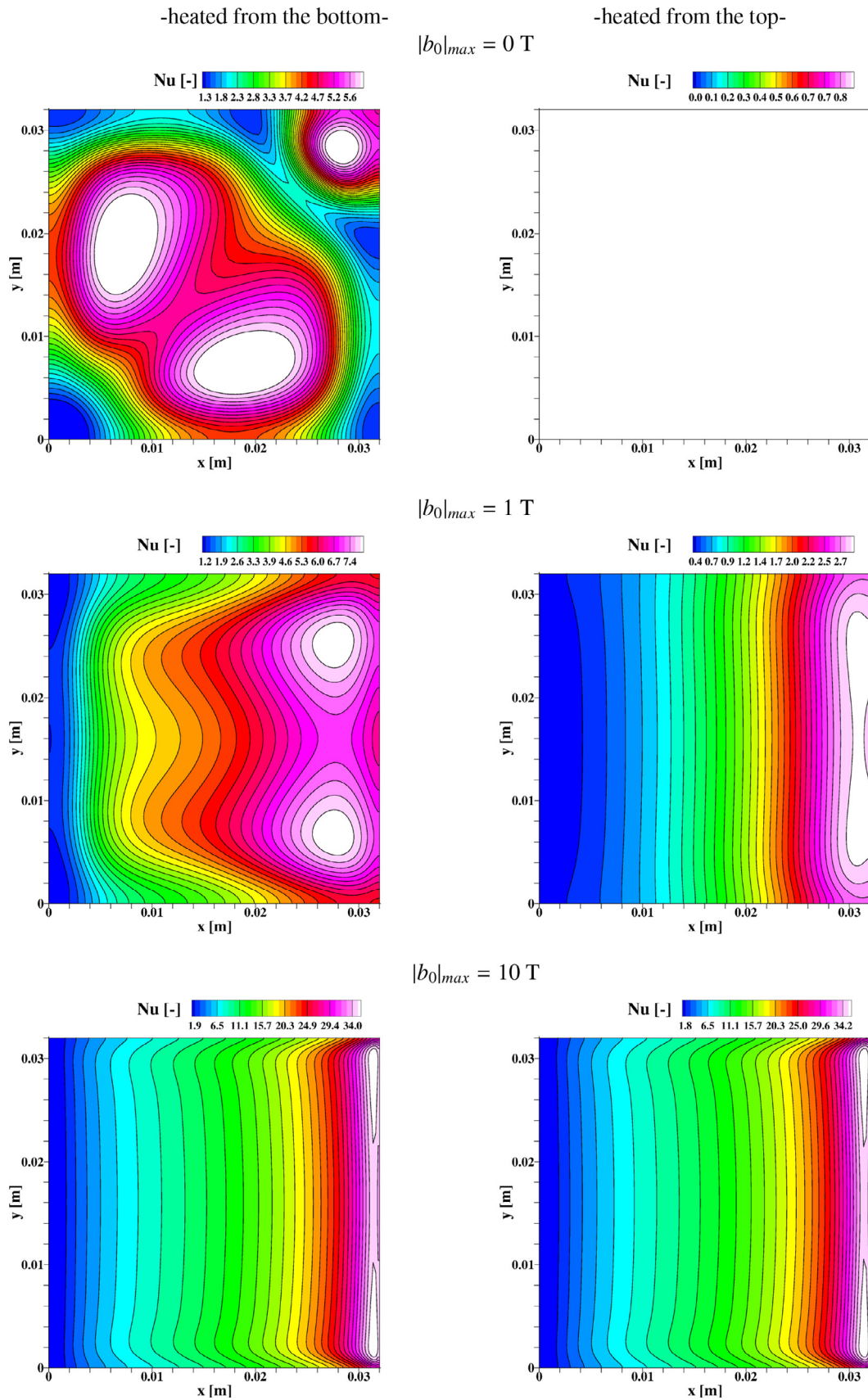


Fig. 5. Contours of the local Nusselt number at the heated horizontal wall for different strengths of the imposed magnetic field, $|b_0| = 0, 1, 10 \text{ T}$. A cube heated from: below (-left), above (-right). Note that different color-scales are used for different cases and that for the neutral heated from the top case, the resulting local values of Nu are equal to one (the pure conduction regime).

wall for both configurations are shown in Fig. 5. For the neutral situation of the heated-from-the-bottom configuration, contours of the local Nusselt number at the lower wall show a diagonal symmetrical distribution, Fig. 5-top/left. Three distinct locations with maximum values are observed. With an increase of the imposed magnetic field strength to $|b_0|_{\max} = 1$ T, this diagonal symmetry is replaced with a horizontal symmetry along the $y = 0.016$ m line. Two characteristic areas with local maxima of Nusselt numbers are visible, Fig. 5-middle/left. Finally, for the highest applied magnetic field ($|b_0|_{\max} = 10$ T), the Nusselt number shows almost uniform distribution along the y -direction indicating a very efficient mixing, Fig. 5-bottom/left. The Nusselt number distributions for heated from above configuration show less distinct changes with magnetic field increase, Fig. 5-right. For this configuration, the horizontal symmetry distribution is already present for $|b_0|_{\max} = 1$ T case, Fig. 5-right/middle. For the highest applied magnetic field, there is almost no difference between the top-heated and bottom-heated configurations, indicating dominance of the magnetization force over the gravitational thermal buoyancy, as can be seen in Fig. 5-bottom. To understand the mechanism behind distributions described above of the local Nusselt number at the hot wall, we will focus on portraying three-dimensional spatial distributions of temperature and velocity fields, obtained from numerical simulations. Before doing so, we will analyze the temporal behavior of the integral heat transfer to confirm that we are dealing with a fully developed, statistically steady, laminar flow regime.

4.2. Temporal evolutions

The time-evolution of the integral Nusselt number for different values of the imposed magnetic field for both configurations, is shown in Fig. 6. Note that we show only the first 15% of the simulated time interval (with a total of three hours of real time to be sure that flow is indeed keeping stable). Immediately after the heat source activation, a significant drop in the Nusselt number values is observed, which is caused by reduction of the highest temperature differences between walls and enclosure interior (which was set to the initial reference temperature). After reaching a local minima, the Nusselt number starts to increase, which is consequence of the generated convective heat transfer (onset of convection). It can be seen that stable values of the integral heat transfer are obtained for both configurations after an initial adjustment period. This adjusting period is significantly shortened when the external magnetic field was applied. For both configurations, a linear increase in Nusselt number is obtained when the magnetic field strength is larger than 5 T. The time-dependencies of the maximum of velocity components are shown in Figs. 7 and 8. All simulations are started with an initial zero velocity field. After a relatively short initial period of flow development ($t \approx 200$ s) a steady non-oscillatory flow regime is established for active magnetic field cases. This initial period is considerably longer for the neutral case. Here, the onset of convection starts at $t \approx 250$ s and the steady flow regime is established after $t \approx 500$ s. There are some important differences in time evolutions of the velocity components for two considered configurations. The vertical velocity component for the bottom-heated configuration shows just a slight variation in $0 \leq |b_0| \leq 4$ T range, Fig. 7a. After that, a linear increase is obtained in the $5 \leq |b_0|_{\max} \leq 10$ T range. In contrast to that, for heated from the top configuration, both horizontal and velocity components exhibit a linear increase, as shown in Fig. 7b. The spanwise velocity component is the smallest among the three components. It is interesting to observe that for the bottom-heated configuration, the magnetization forcing initially suppresses the spanwise velocity and only for the strongest magnetic field it reaches values of its neutral state, as can be seen Fig. 8a. For the top-heated situation, the spanwise velocity exhibits monotonic linear increase, Fig. 8b.

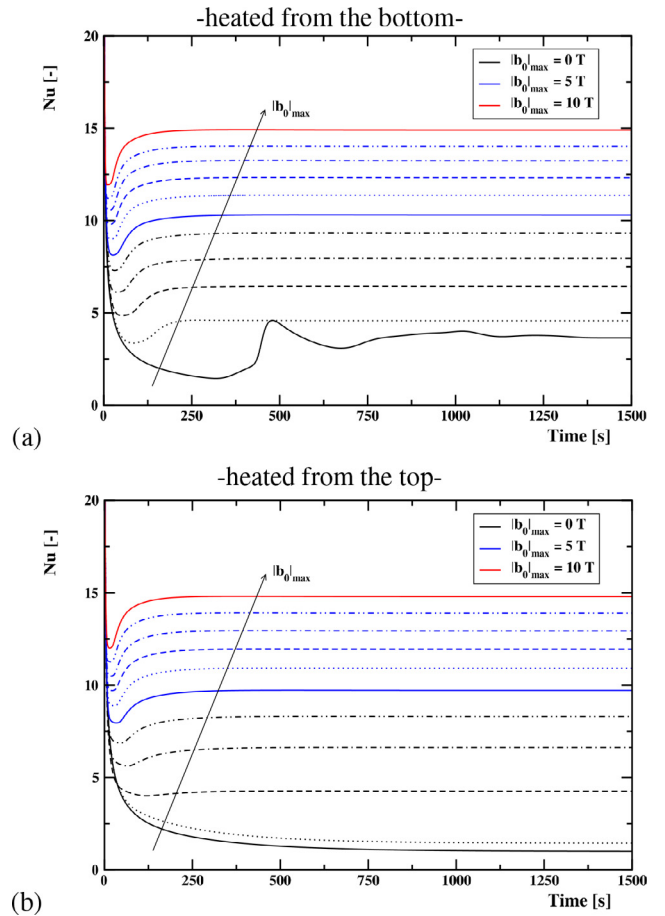


Fig. 6. Time evolution of the integral Nusselt number over the heated wall for two configurations and different strengths of the imposed magnetic field, $0 \leq |b_0|_{\max} \leq 10$ T.

Based on the presented temporal evolutions of integral heat transfer and maximal values of the velocity components, it is confirmed that stable laminar flow regimes are observed for both configurations.

4.3. 3D features of flow and temperature field

The isosurfaces of non-dimensional temperature ($\theta^* = (\theta - \theta_c)/(\theta_h - \theta_c)$, in total 15 values) for both configurations are shown in Fig. 9. For the top-heated configuration, the initially stable stratified temperature field in the vertical direction is gradually evolving in the horizontally stratified configuration with an increase of the imposed magnetic field, Fig. 9-right. The bottom-heated configuration exhibits more significant reorganization of the temperature field, Fig. 9-left. It can be seen that the local maximum of the Nusselt number in the top/right corner of the bottom wall shown in Fig. 5-top/left, is caused by a downward oriented thermal plume along $x = 0.032$ and $y = 0.032$ m corner, Fig. 9-top/left. Similarly, the remaining two peaks in Nusselt number coincide with even stronger downdrafts in the central part of the enclosure. This three-downdrafts structure is replaced with a two-downdrafts structure for $|b_0|_{\max} = 1$ T, Fig. 9-middle/left. Finally, the centrally located thermal plumes are not visible any more for the highest value of $|b_0|_{\max} = 10$ T, Fig. 9-bottom/left. The final state is characterized by a stable horizontal thermal stratification in the central part of the enclosure and by thermal boundary layers created along the horizontal walls. To illustrate characteristic flow patterns, the streamtraces of the massless particles (which are uniformly

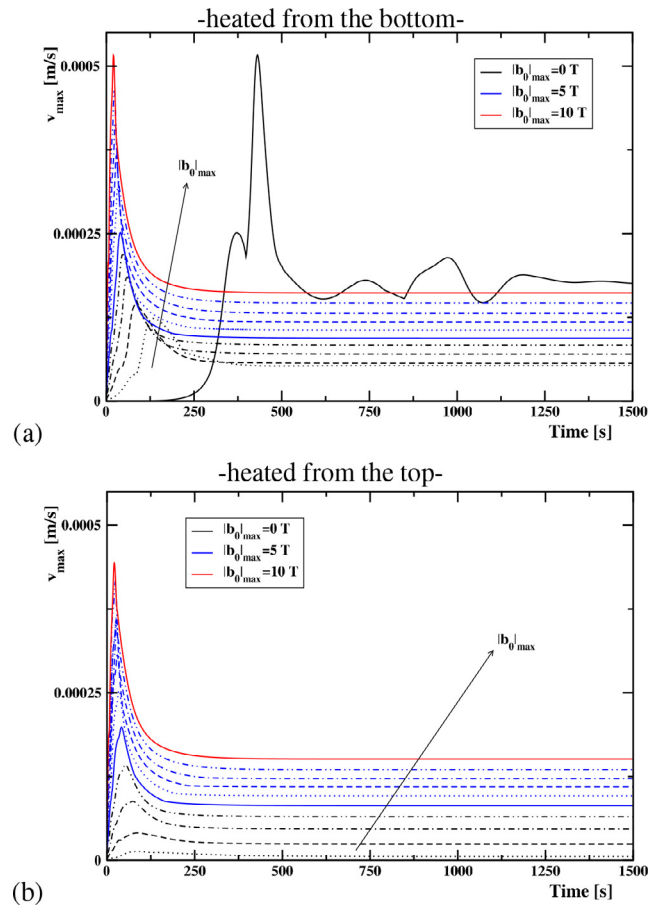
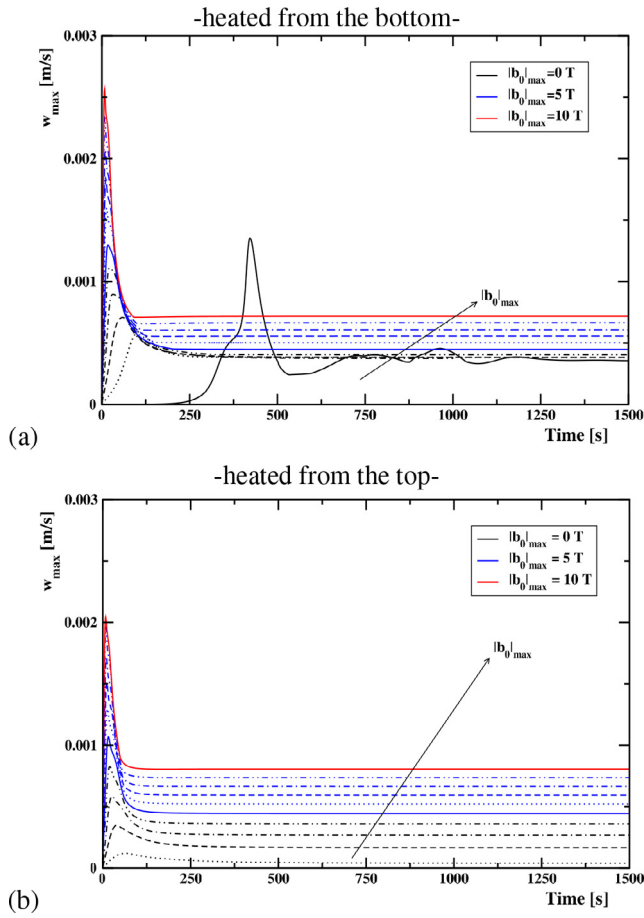


Fig. 7. Time evolution of the maximal vertical (in the z -direction) velocity for two configurations and different intensities of imposed magnetic field, $0 \leq |b_0|_{\max} \leq 10$ T. Note that for the neutral heated from the top case there is no flow generated.

Fig. 8. Same as in the previous figure, now for the v_{\max} (spanwise, in the y -direction) velocity component. Note that for the neutral heated from the top case there is no flow generated.

released in the central vertical line ($x = 0.016$ m, $y = 0.016$ m, $0 \leq z \leq 0.032$ m) and traced in time with the 4th order Runge-Kutta method) are presented in Fig. 10. For the neutral bottom-heated configuration, one central anti-clockwise rotating and two smaller clockwise rotating rolls are perfectly aligned with the main diagonal of the cube, Fig. 10-top/left. This flow alignment is already disappearing with the imposition of a weak magnetic field ($|b_0|_{\max} = 1$ T), Fig. 10-middle/left. Now, a centrally located clockwise rotating roll structure is generated. In contrast to that, for the top-heated situation, two anticlockwise rotating rolls are generated in the central vertical plane, Fig. 7-middle/left. For the highest imposed magnetic field ($|b_0|_{\max} = 10$ T), two-distinct rotating cells are generated again in the proximity of the lower and upper horizontal wall and are spatially extended along the y -coordinate direction, Fig. 10-bottom. The structure of the flow is now almost the same for both configurations - the only difference is in the direction of rotation. Finally, we conclude that the imprints of the flow structures are directly correlated with the local distributions of the wall heat transfer shown in Fig. 5.

4.4. Dissimilarity between the flow and heat transfer: streamtraces and heat flux lines

The superimposed contours of the non-dimensional vertical velocity and two-dimensional streamtraces in the central vertical plane are shown in Fig. 11. For the neutral bottom-heated case, the streamtraces portray a large central anti-clockwise rotating vortex in combination with two weak circulation regions along the side

walls, Fig. 11-top/left. Even with a slight increase in the magnetic field strength, the streamtraces indicate a change in the direction of the central vortex, which is now rotating clockwise, and without the side-wall recirculations, Fig. 11-middle/left. With further increase of the imposed magnetic field, the recirculation in the central part weakens and two recirculating patterns are moved towards the thermally active walls with a simultaneous decrease in thickness of the wall-jets in the proximity of the thermally active horizontal walls, Fig. 11-bottom/left. This flow pattern corresponds now very closely for a typical side-heated cubical enclosure scenario, i.e., the flow is practically rotated by 90° when compared to its initial state. For the top-heated situation, after the initially stable regime (Fig. 11-top/right), the flow is already generated at $|b_0|_{\max} = 1$ T, with two anti-clockwise rotating vortices, Fig. 11-middle/right. Finally, for the highest imposed magnetic field, the flow pattern is very similar to the bottom-heated situation when mirrored in respect to the center of the x -axis, confirming the dominance of the magnetization force, Fig. 11-bottom/right.

The superimposed contours of the non-dimensional temperature and corresponding two-dimensional heat flux lines for both configurations are shown in Fig. 12. The heat flux lines are created similarly to the streamtraces, but instead of using the velocity components, the convection and diffusion components of the heat-flux are used, i.e. $q_i = u_i\theta - a\partial\theta/\partial x_i$. Then, the identical tracing algorithm used to plot the streamtraces is applied to plot the heat flux isolines. Note that the heat flux lines approach applied here does not require any additional solving of the heat function, Costa [19], nor is this approach restricted to the two-dimensional

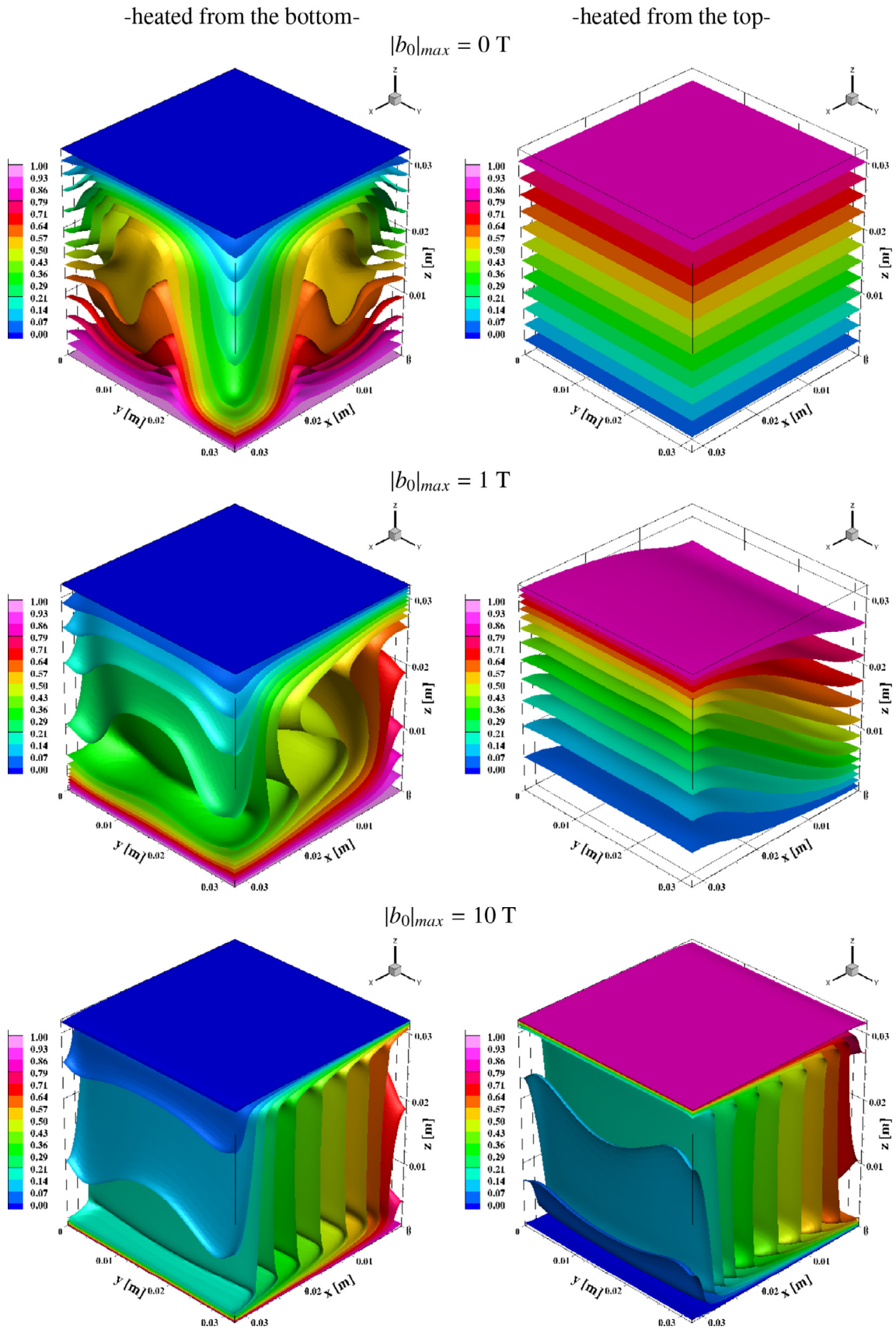


Fig. 9. Iso-surfaces of non-dimensional temperature ($\theta^* = (\theta - \theta_c)/(\theta_h - \theta_c)$) for different strengths of the imposed magnetic field ($|b_0| = 0, 1, 10\text{ T}$), left- heated from the bottom, right- heated from the top.

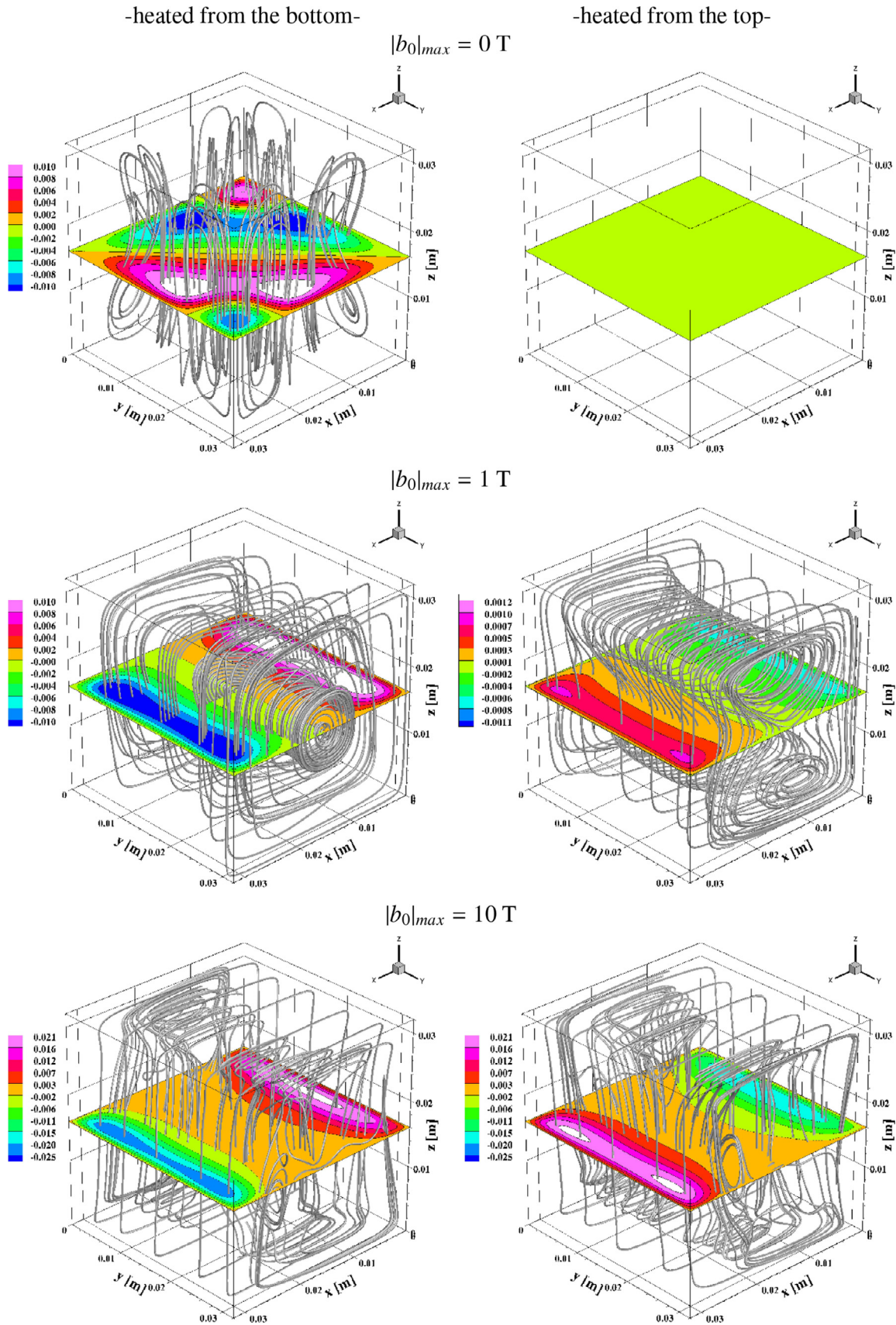


Fig. 10. The contours of the non-dimensional vertical velocity (w/V_b , where $V_b = \sqrt{\beta g \Delta \theta H}$ is the buoyancy velocity) in the central horizontal plane and streamtraces of the massless particles for different strengths of the imposed magnetic field ($|b_0| = 0, 1, 10 \text{ T}$), left- heated from the bottom, right- heated from the top.

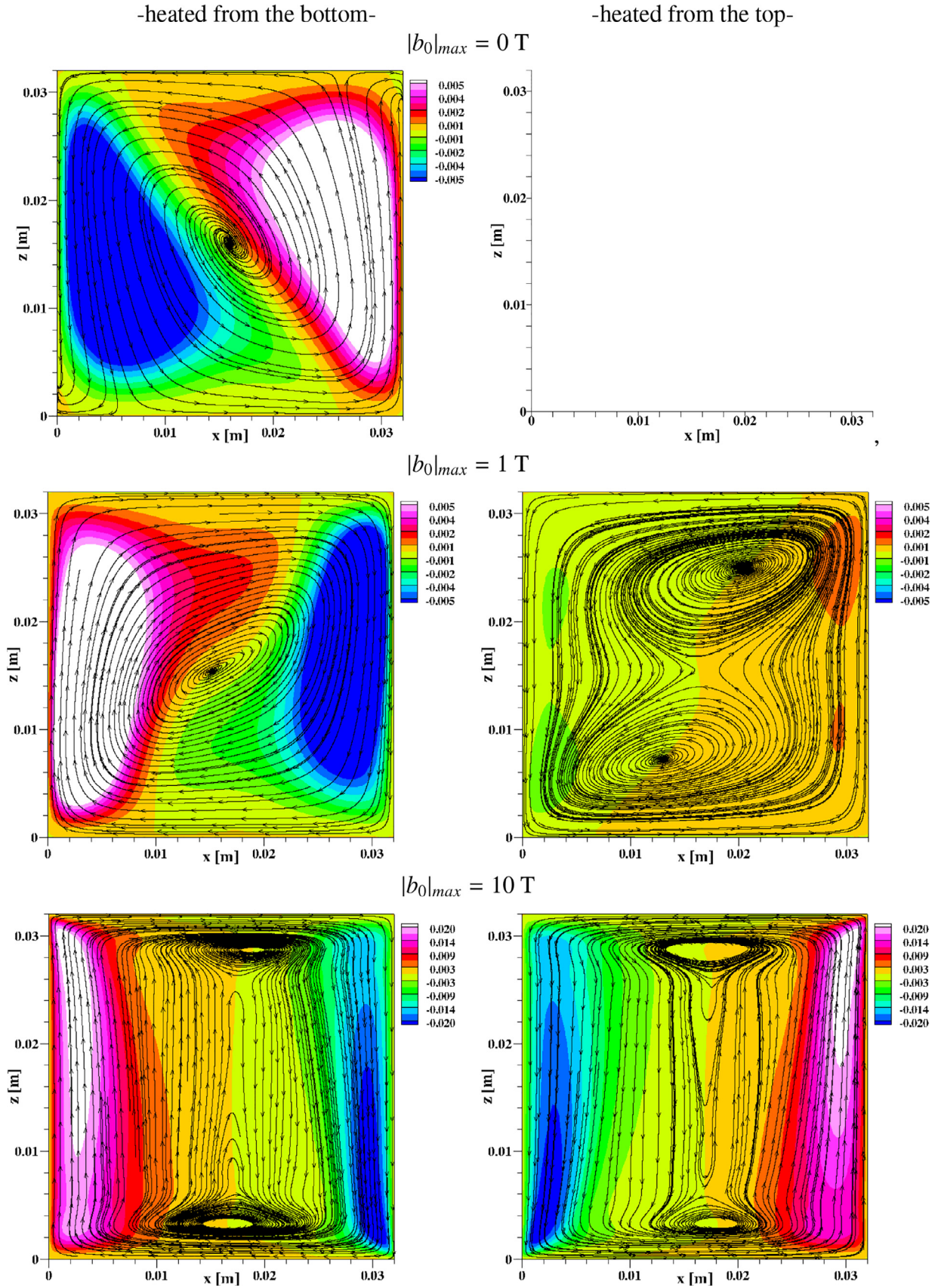


Fig. 11. Superimposed streamtraces and contours of the non-dimensional vertical velocity ($w^* = w/\sqrt{\beta g \Delta \theta H}$) in the central vertical plane for different strengths of the imposed magnetic field for both configurations: heated from the bottom (-left) and heated from the top (-right).

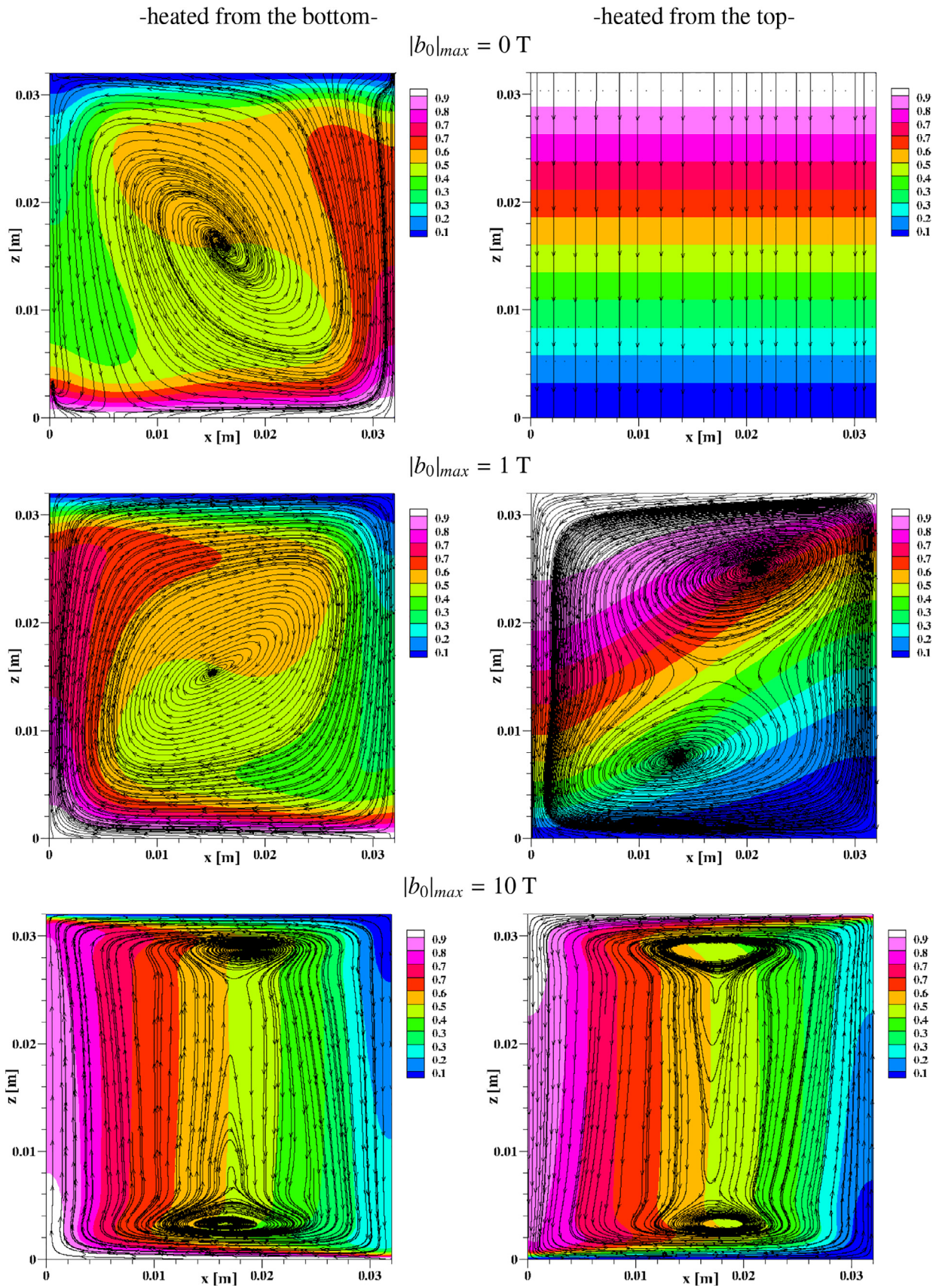


Fig. 12. Superimposed contours of the non-dimensional temperature ($\theta^* = (\theta - \theta_c)/(\theta_h - \theta_c)$) and heat flux lines (calculated from components of the total heat flux, $q_i = \theta u_i - a\partial\theta/\partial x_i$) in the central vertical plane for different values of imposed magnetic field and two configurations.

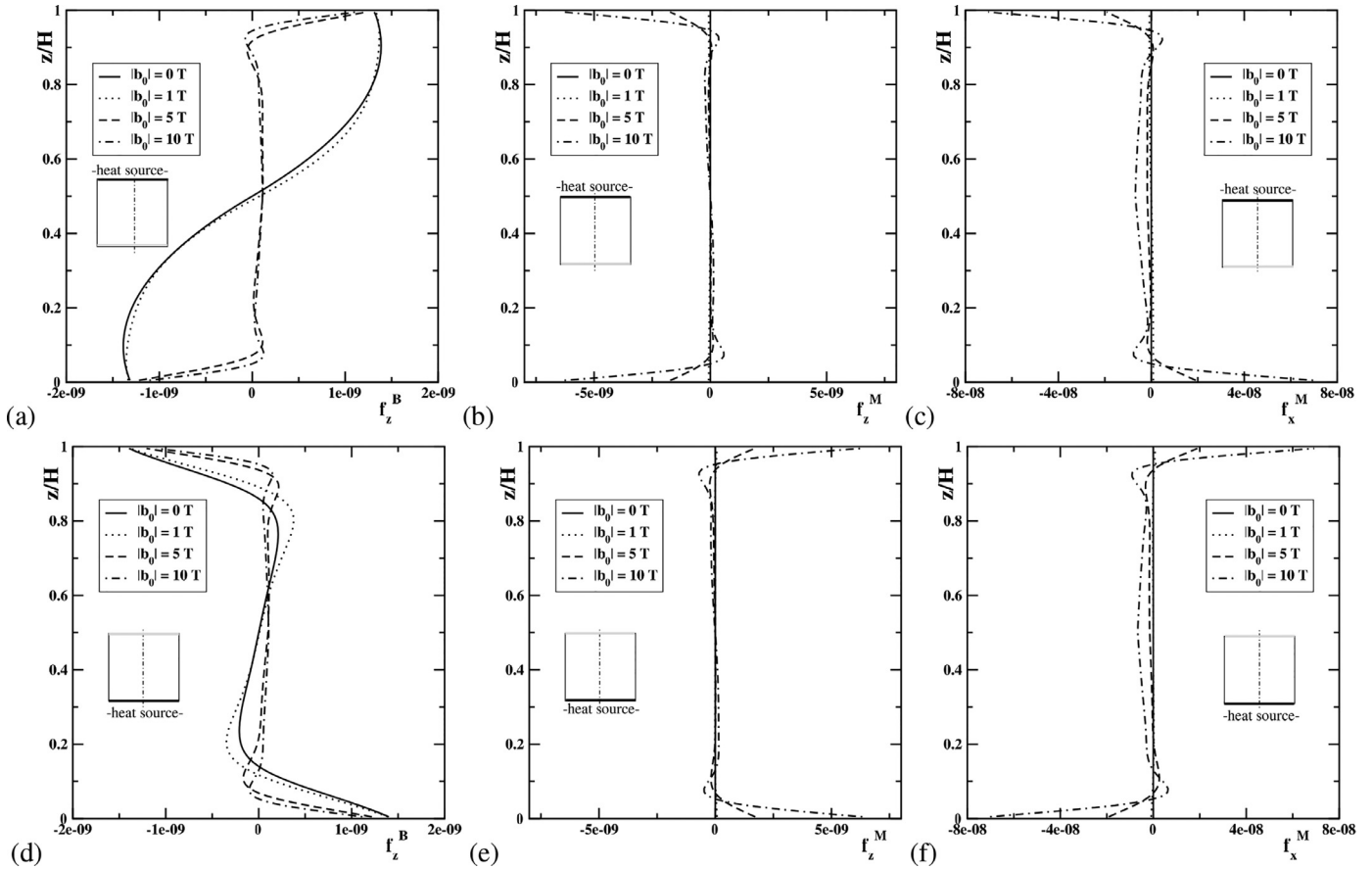


Fig. 13. Vertical profiles of the thermal buoyancy (Eq. (5)) and dummyTXdummy-(of the magnetization force (Eq. (6)) (both integrated over the control volume and multiplied with the density of working fluid, i.e. $f_i \cdot \Delta V \cdot \rho$, with the final values in N) in the central vertical plane ($y/D = 0.5$, $x/L = 0.5$) for different strengths of the imposed magnetic field ($|b_0|_{\max} = 0, 1, 5, 10$ T), above-heated from the top ((a)- f_z^B , (b)- f_z^M , (c)- f_x^M), below-heated from the bottom ((d)- f_z^B , (e)- f_z^M , (f)- f_x^M).

divergence-free situations. For the neutral top-heated case, there is no flow and the heat flux lines are simply represented as a straight lines from top to bottom, Fig. 12-top/right. For heated from the bottom situation, the heat flux lines exhibit a similar behavior to the streamtraces in the central part of the cube, whereas the diffusion important regions are located in the proximity of the horizontal walls, Fig. 12-top/left. With further increase of the imposed magnetic field strength, the diffusion dominant regions become smaller, indicating the reduction of the thickness of thermal boundary layers in the proximity of the horizontal walls, Fig. 12-middle. Finally, the heat flux lines distribution is very similar for both configurations, for the highest applied magnetic field, Fig. 12-bottom.

4.5. Local analysis of the thermal buoyancy and magnetization forces

To explain the directions of flow patterns obtained, we focus on plotting characteristic profiles of the magnetization and thermal buoyancy forces (given in Eqs. (6) and (7)) (integrated per control volume) in the central vertical plane for both configurations considered, Fig. 13. Note that in contrast to the thermal-buoyancy (gravitational) force, which is characterized by one-dimensional dependency (in the z -direction), the magnetization force shows a multi-dimensional character (due to the existence of the magnetic field gradients in all three coordinate directions). It can be seen that the gravitational force distribution is just slightly adjusted for the top-heated case when the magnetic field is switched on, Fig. 13a. With further increase of the magnetic field, the values of the gravity force drop to zero in the central part of the box,

with significant contributions in the proximity of the top and bottom walls. For heated from the bottom case, the gravitational force does not exhibit a change of the sign with magnetic field increase, Fig. 13d. For both situations, the magnetization force is of opposite sign to the gravitational force, Fig. 13b and e and are dominant forces in the system for intermediate and large values of magnetic field strength. The distribution of the horizontal magnetization forces provides a key to understanding the direction of the flow rotation, as can be seen from Fig. 13c and f.

5. Conclusions

We demonstrated that upon the action of the magnetization force, the direction of the flow and heat transfer of a paramagnetic fluid in a differentially heated cubical enclosure subjected to a strong magnetic gradient of a superconducting magnet can be inverted. For both configurations of the initial thermal stratification analyzed, i.e. heated from the bottom or heated from the top at a fixed value of $Ra = 1.4 \times 10^5$ and $Pr = 584$, significant heat transfer enhancements up to 5 and 15 times, respectively, were obtained in comparison with the neutral (no magnetic field) cases. Measured and numerically obtained integral heat transfer showed a good agreement over an entire range of imposed magnetic fields. In addition, the numerical simulations provided detailed insights into three-dimensional velocity and temperature, as well as of the local distributions of the thermal buoyancy (gravitational) and magnetic buoyancy (magnetization) forces.

Declaration of Competing Interest

The authors declare that they have no known competing financial interests or personal relationships that could have appeared to influence the work reported in this paper.

Acknowledgments

S. K. acknowledges the Marie Curie Visiting Professorship at AGH University of Science and Technology, Krakow, Poland.

Supplementary material

Supplementary material associated with this article can be found, in the online version, at [10.1016/j.ijheatmasstransfer.2020.119407](https://doi.org/10.1016/j.ijheatmasstransfer.2020.119407)

References

- [1] D. Braithwaite, E. Beaugnon, R. Tournier, Magnetically controlled convection in a paramagnetic fluid, *Nature* 354 (1991) 134–136.
- [2] H. Ozoe, *Magnetic Convection*, Imperial College Press, London, U.K., 2005.
- [3] J. Qi, N.I. Wakayama, A. Yabe, Magnetic control of thermal convection in electrically non-conducting or low-conducting paramagnetic fluids, *Int. J. Heat Mass Transf.* 44 (2001) 3043–3052.
- [4] T. Tagawa, R. Shigemitsu, H. Ozoe, Magnetization force modeled and numerically solved for natural convection of air in a cubic enclosure: effect of the direction of the magnetic field, *Int. J. Heat Mass Transf.* 45 (2002) 267–277.
- [5] T. Tagawa, A. Ujihara, H. Ozoe, Numerical computation for Rayleigh-Bénard convection of water in a magnetic field, *Int. J. Heat Mass Transf.* 46 (2003) 4097–4104.
- [6] R. Shigemitsu, T. Tagawa, H. Ozoe, Numerical computation for natural convection of air in a cubic enclosure under combination of magnetizing and gravitational forces, *Numer. Heat Transf. Part A* 43 (5) (2003) 449–463.
- [7] P. Filar, E. Fornalik, M. Kaneda, T. Tagawa, H. Ozoe, J. Szmyd, Three-dimensional numerical computation for magnetic convection of air inside a cylinder heated and cooled isothermally from a side wall, *Int. J. Heat Mass Transf.* 48 (2005) 183–191.
- [8] T. Bednarz, E. Fornalik, T. Tagawa, H. Ozoe, J.S. Szmyd, Experimental and numerical analysis of magnetic convection of paramagnetic fluid in a cube heated and cooled from opposing vertical walls, *Int. J. Therm. Sci.* 44 (2005) 933–943.
- [9] T. Bednarz, E. Fornalik, H. Ozoe, J.S. Szmyd, J.C. Patterson, C. Lei, Influence of a horizontal magnetic field on the natural convection of paramagnetic fluid in a cube heated and cooled from two vertical side walls, *Int. J. Therm. Sci.* 47 (2008) 668–679.
- [10] T. Bednarz, J.C. Patterson, C. Lei, H. Ozoe, Enhancing natural convection in a cube using a strong magnetic field - experimental heat transfer rate measurements and flow visualization, *Int. Commun. Heat Mass Transf.* 36 (2009) 781–786.
- [11] W. Wrobel, E. Fornalik-Wajs, J.S. Szmyd, Experimental and numerical analysis of thermo-magnetic convection in a vertical annular enclosure, *Int. J. Heat Fluid Flow* 31 (6) (2010) 1019–1031.
- [12] S. Kenjereš, L. Pyrda, W. Wrobel, E. Fornalik-Wajs, J.S. Szmyd, Oscillatory states in thermal convection of a paramagnetic fluid in a cubical enclosure subjected to a magnetic field gradient, *Phys. Rev. E* 85 (046312) (2012) 1–8.
- [13] S. Kenjereš, L. Pyrda, E. Fornalik-Wajs, J.S. Szmyd, Numerical and experimental study of Rayleigh-Bénard-Kelvin convection, *Flow Turbul. Combust.* 92 (1–2) (2014) 371–393.
- [14] D.R. Lide, W.M. Haynes, *CRC Handbook of Chemistry and Physics*, The 91st Edition, 2010, CRC Press, Boca raton, Florida, U.S.A.
- [15] S.W. Churchill, H. Ozoe, Correlations for laminar free convection from a vertical plate, *J. Heat Transf. Trans. ASME* 95 (4) (1973) 540–541.
- [16] J.J. David, *Classical Electrodynamics*, third ed., Willey, New York, 1999.
- [17] S. Kenjereš, On modeling and eddy-resolving simulations of flow, turbulence, mixing and heat transfer of electrically conducting and magnetizing fluids: a review, *Int. J. Heat Fluid Flow* 73 (2018) 270–297.
- [18] G. Grötzbach, Spatial resolution requirements for direct numerical simulation of the Rayleigh-Bénard convection, *J. Comput. Phys.* 49 (1983) 241–264.
- [19] V.A.F. Costa, Bejan's heatlines and masslines for convection visualisation and analysis, *Appl. Mech. Rev.* 59 (2006) 126–145.